# Hierarchical Design of CuS Architectures for Visible Light Photocatalysis of 4-Chlorophenol

Sangeeta Adhikari,[†] Debasish Sarkar,[‡] and Giridhar Madras[*,†]

[†]Department of Chemical Engineering, Indian Institute of Science, Bangalore 560012, Karnataka, India
[‡]Department of Ceramic Engineering, National Institute of Technology, Rourkela 769008, Odisha, India

ABSTRACT: Hydrothermal-assisted CuS hierarchical architectures were grown in the presence of anionic sulfur sources, and the investigation of their degradation efficiency for a pesticide 4-chlorophenol (4-CP) under visible light irradiation was carried out. The dissociation of S^{2-} from the sulfur compound governs the nucleation of CuS followed by a specific pattern of growth to produce different morphologies. The self-assembled covellite spherical CuS flower architecture assembles in the presence of thiourea and exhibits the highest photodegradation activity. The open architecture of ~2.3 μm spherical CuS flowers consisting of a ~100 nm thick sheet encompasses a comparatively high surface area and particle growth along the (110) plane that facilitates more active sites for catalytic activity enhancement. The catalyst loading for 4-CP degradation has been optimized, and a detailed trapping mechanism has been explored.
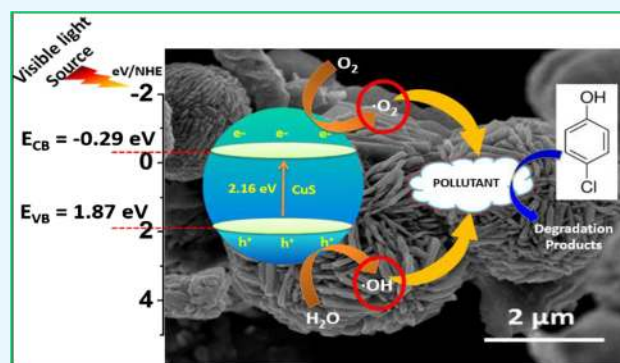
1. INTRODUCTION

High resistance of organic contaminants toward the conventional biological and chemical treatments demands a sustainable approach for treatment of wastewater to facilitate the recycling and reuse of wastewater.[1] The advanced treatment technologies such as chemical precipitation, adsorption, advanced oxidation processes (AOPs), electrochemical oxidation, and membrane processes are efficiently able to destroy the persistent organic pollutants.[2,3] Recent research focuses on the heterogeneous photocatalytic AOPs for its enhanced degradation efficiency with generation of benign products nonselectively.[4] AOPs require light for photocatalysis to enhance the activity through Fenton process.[5] The catalytic efficiency of the photo-Fenton process is pH-dependent as the precipitate dissolves at pH below 2.8 for the formation of active $[Fe(OH)]^{2+}$ species. The refinement of pH requires high chemical overheads that restrict its utility.[6] Semiconducting metal oxides and sulfides have been extensively researched in the recent years.[7−10] Among them, copper based-chalcogenides impart unique physical, chemical, electrical, and optical properties with synergistic contribution in the field of optoelectronic devices, energy storage, biosensors, lithium ion batteries, solar cells, and photocatalysis.[11−13]

Covellite CuS is an interesting material that has been recognized owing to its ability to absorb solar spectra in the visible region. The micro/nano-CuS semiconductor has been explored for the degradation of organic dyes.[14,15] Basu et al. reported the disintegration of different organic dye pollutants through hexagonal-stacked CuS plates under indoor lighting.[16] CuS-caved superstructures were fabricated by Shu et al. for dye degradation.[17] Dye degradation was also performed by CuS

nanofibers that were synthesized with the assistance of polyacrylonitrile.[18] A chemically dealloyed CuS photocatalyst was investigated for the photodegradation of azo dyes.[19] The photocatalytic efficiency of these copper chalcogenides depends on factors such as material design (morphology, size, and surface area), tuning optical absorption, and surface modification by doping or forming heterojunctions.[20,21] To achieve the desired property, strategies toward synthesis also play a pivotal role.[22] To control the design of materials, efforts have been made through methodologies such as coprecipitation, solvothermal synthesis, hydrothermal synthesis, and hot injection.[23,24] The hierarchical self-assembled structures enhance the performance of materials through micro- or nano-sized building blocks.[25] Therefore, the investigation of hierarchical semiconductor microarchitectures built from nano building blocks is of utmost significance for both scientific and industrial applications. Studies report that the different sulfur sources in varying base precursors of copper (nitrates, chlorides, and acetates) forms versatile microstructures.[9,26,27] However, a comparative morphology-driven photocatalytic study of CuS, derived from a common precursor with different sulfur sources, has not been reported.

Considering the gradient of major pollutants other than dyes, chlorinated phenols pose a serious threat to ecological system as they are toxic, suspected to be carcinogenic, and recalcitrant.[28,29] Among the chlorinated phenols, 4-chlorophe-

nol (4-CP) is a potential toxin that has direct relevance to the environmental pollution.[30] The impact of material designing onto photocatalytic degradation of 4-CP has not been reported before. The present investigation has been directed toward the design of different CuS photocatalysts by a facile hydrothermal method by using different sulfur sources, and the study of their morphological evolution was carried out. The as-prepared CuS photocatalysts have been evaluated for the photocatalytic activity toward degradation of 4-CP under visible light illumination.

2. RESULTS AND DISCUSSION

2.1. Structural, Morphological, and Optical Analysis.
The X-ray diffraction (XRD) patterns of the synthesized CuS powders, designated as CuS-ST, CuS-TA, and CuS-TU, are presented in Figure 1a, which provides an insight to the
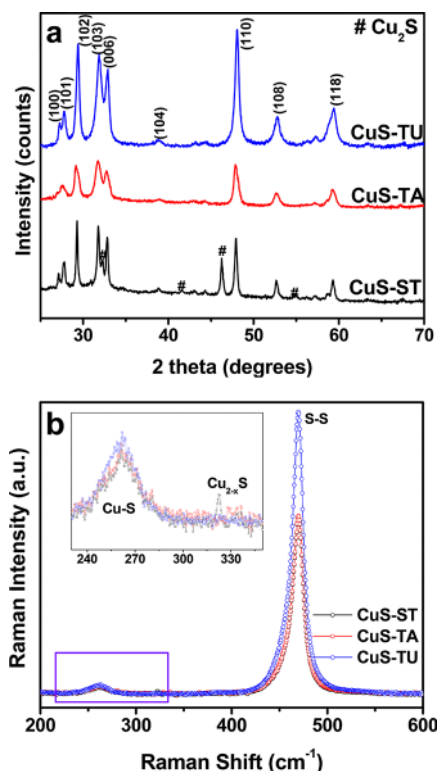

Figure 1. (a) XRD patterns with varying directing agents (CuS-ST, CuS-TA, and CuS-TU) and (b) composite Raman spectra of CuS microstructures.

crystallinity, purity, and phase of the products. All of the diffraction peaks could be well-indexed to the hexagonal covellite CuS crystal phase that matches well with the JCPDS card no. 24-0060 having cell parameters, $a = b = 3.796$ Å and $c = 16.360$ Å and a space group of $P6_3/mmc$. The intense and sharp diffraction peaks are obtained that suggest high crystallinity of the powders. From the XRD patterns, it is evident that the resultant product of CuS-ST has a phase mixture of hexagonal covellite and cubic digenite (Cu_2S, 02-1287, marked as # in the figure), whereas CuS-TA and CuS-TU do not have any other phase that suggests high purity of both the powders synthesized by thioacetamide and thiourea sources, respectively. The formation of Cu_2S can be attributed to desulfurization of CuS to Cu_2S under high pressure.[31] The covellite peaks of CuS-TU have been indexed to (100), (101),
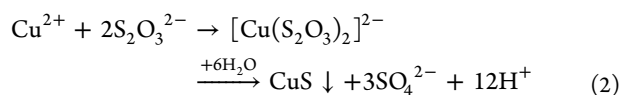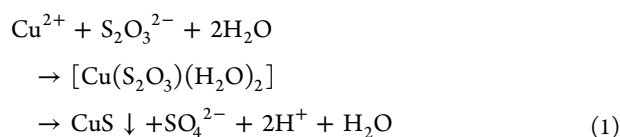
(102), (103), (006), (104), (110), (108), and (118). Although there is no peak shifting, it could be observed that the peaks obtained for CuS-TU are sharper than the peaks obtained for both CuS-ST and CuS-TU, which indicates that the particles are highly crystalline in CuS-TU. A thorough examination of the diffraction pattern reveals that the diffraction intensity of the peak (103) is lower than that in the standard JCPDS pattern. However, the intensity of (110) peak in particular is very high, which is indicative of the preferred growth along the (110) plane in the crystalline powder. This particular plane can be attributed to have played a major role in the morphology formation, which can be further understood from the detailed transmission electron microscopy (TEM) analysis.

Atomic vibrational modes identifying the surface species and spatial variations in composition are known from Raman measurement of the samples. Typical Raman spectra of the as-prepared powders are shown in Figure 1b. All of the spectra show a sharp and intense peak at 473 cm^{-1}, which can correspond to the vibrational mode from covalent S−S bonds of S_2 ions at the 4e sites.[32] This sharp peak indicates that the lattice atoms are aligned in the periodic array. Other than this sharp peak, a broad Raman peak at 266 cm^{-1} is observed that is due to the vibration from Cu−S bond. An additional peak is also observed in the Raman spectra of CuS-ST at wavenumber of 322 cm^{-1}, which can be assigned to the $Cu_{2-x}S$ (where, x varies from 0, $6 \leq x \leq 1$) phonon mode as Raman scattering is sensitive toward the defect crystal phases.[33] In the present case, the value of $x = 0$, as also observed from the XRD analysis. The Raman data support the formation of pure structure of CuS in CuS-TA and CuS-TU and also support the formation of defect Cu_2S in CuS-ST.

The morphology of CuS powders has been investigated by field emission scanning electron microscopy (FESEM), and the images are presented in Figure 2a−c for CuS-ST, CuS-TA, and CuS-TU, respectively. Figure 2a shows the image of as-synthesized CuS-ST powders that has an elongated one-dimensional structure. In contrast to the one-dimensional structures formed, few bundled flaky structures are also observed that is composed of numerous elongated ferns. This suggests that the one-dimensional structure is shaped as a result of self-assembly and rearrangement of these flaky forms. A closer view of the elongated structure indicates that the sheets have assembled as a result of nucleation and growth process to form an intrinsic anisotropic structure. The average diameter of the one-dimensional structure has been calculated to be ~35 nm. The hexagonal CuS sheets consist of alternating layers of CuS and Cu_2S_2 as composites held by weak van der Waals forces that the crystal can effortlessly cleave and obtain the smooth surface.[34] The aggregation and arrangements of these sheets along an oriented direction are governed by the factors such as concentration of precursors, reaction time, and also the source of sulfur in the reaction. The chemical reaction occurring in the presence of $Na_2S_2O_3$ is that $S_2O_3^{2-}$ ions in the solution combines with Cu^{2+} ions to form $[Cu(S_2O_3)\cdot 2(H_2O)]$ and $[Cu(S_2O_3)_2]^{2-}$ complexes in water at room temperature. CuS is formed upon reaction between Cu/Cu^{2+} ions produced from the dissociated complex and S^{2-} ions formed as a result of hydrolysis as shown in the equations (eqs 1 and 2) below[35]
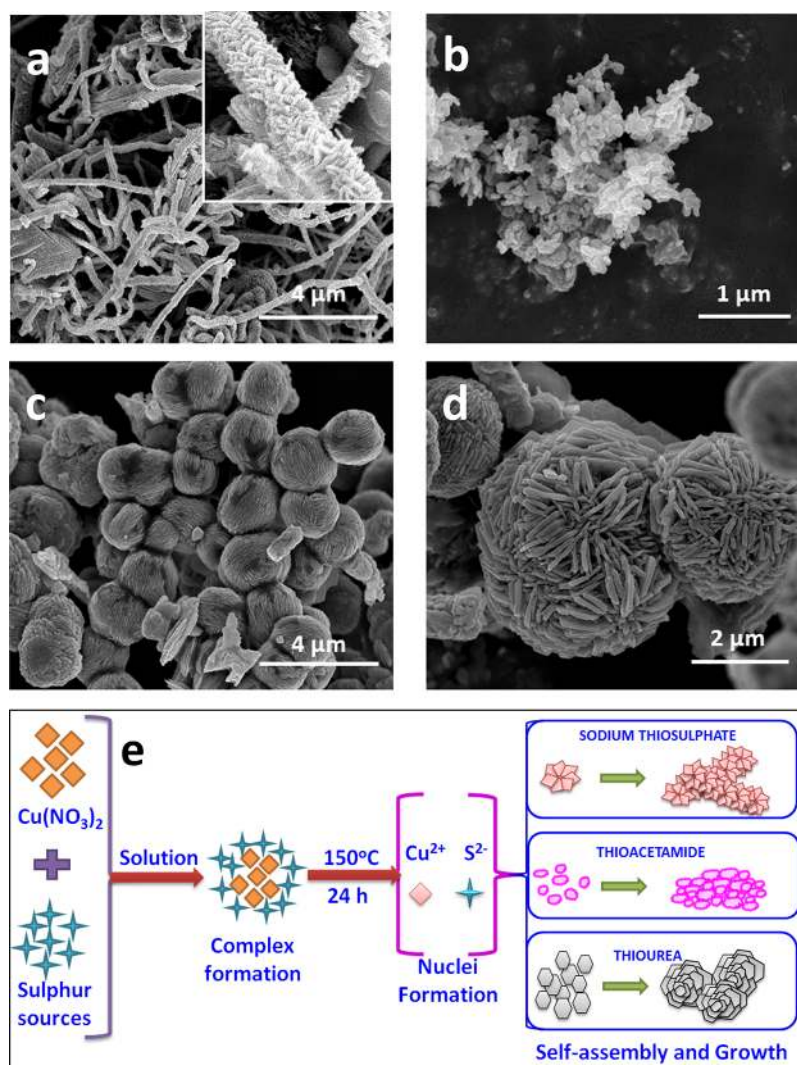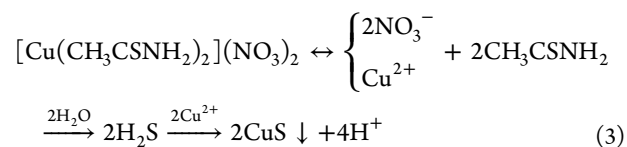
Figure 2. FESEM images of (a) CuS-ST, (b) CuS-TA, (c,d) CuS-TU, and (e) graphical representation of the morphology formation.

$$Cu^{2+} + S_2O_3^{2-} + 2H_2O$$
$$\rightarrow [Cu(S_2O_3)(H_2O)_2]$$
$$\rightarrow CuS \downarrow + SO_4^{2-} + 2H^+ + H_2O \tag{1}$$

$$Cu^{2+} + 2S_2O_3^{2-} \rightarrow [Cu(S_2O_3)_2]^{2-}$$
$$\xrightarrow{+6H_2O} CuS \downarrow + 3SO_4^{2-} + 12H^+ \tag{2}$$

The FESEM image of CuS-TA powder, which uses thioacetamide as a sulfur source, shows flat random set of particles, as observed in Figure 2b. Hydrothermal synthesis of sulfide is related to the coordination between the metal ions and also dissociation of the sulfide precursor. The dissociation of thioacetamide to sulfide ions (S^{2-}) under hydrothermal condition governs the process of nucleation, growth, distribution, and aggregation of the particles. Under acidic condition, thioacetamide dissociates into H_2S via an intermediate product that further dissociates into HS^- and S^{2-}. However, in the present study, the above phenomenon does not occur because the solution is not acidic. It can be presumed that the reaction precursor forms the $[Cu(CH_3CSNH_2)_2]NO_3$ complex that dissociates to corresponding Cu^{2+} and NO_3^{2-} ions along with the CH_3CSNH_2 group. This undergoes
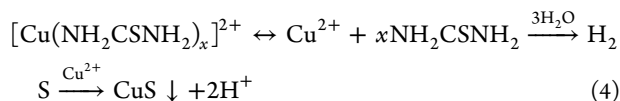
hydrolysis under high temperature and pressure to form H_2S and reacts with the produced Cu^{2+} ions, precipitating CuS. The disordered nucleation/growth followed by the formation of an improper and randomly oriented morphology attributes to the low degree of product yield (~50%) during the thioacetamide-assisted hydrolysis reaction. The probable chemical reaction for the precipitation of CuS in the presence of thioacetamide can be given as follows[36]

$$[Cu(CH_3CSNH_2)_2](NO_3)_2 \leftrightarrow \begin{cases} 2NO_3^- \\ Cu^{2+} \end{cases} + 2CH_3CSNH_2$$
$$\xrightarrow{2H_2O} 2H_2S \xrightarrow{2Cu^{2+}} 2CuS \downarrow + 4H^+ \tag{3}$$

Similar to the complex formation using thioacetamide, thiourea also forms a strong complex in the presence of Cu^{2+} ions and water, which is evident from the change in color of the reaction solution from green to pale white, indicative of the formation of the thiourea−copper(II) complex as shown in the first step of eq 4.[26] However, the precipitation of CuS follows the process similar to that of CuS formed from the hydrolysis of dissociated thioacetamide complex, followed by the reaction with Cu^{2+} ions in the solution.
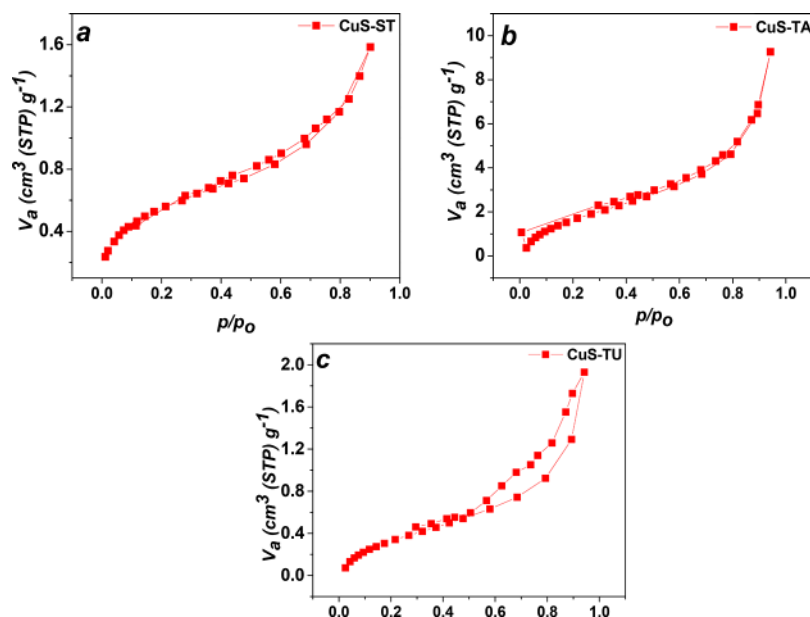
Figure 3. Nitrogen adsorption−desorption BET isotherm of (a) CuS-ST, (b) CuS-TA, and (c) CuS-TU powders.

$$[Cu(NH_2CSNH_2)_x]^{2+} \leftrightarrow Cu^{2+} + xNH_2CSNH_2 \xrightarrow{3H_2O} H_2$$

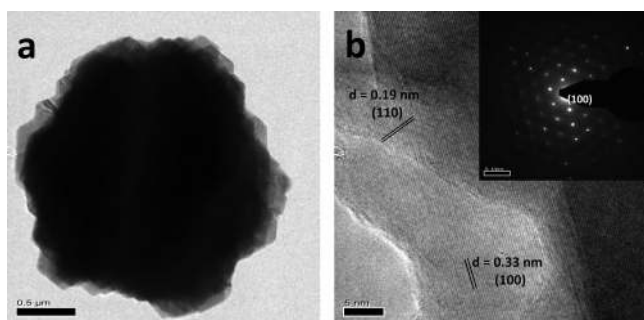$$S \xrightarrow{Cu^{2+}} CuS \downarrow + 2H^+ \qquad (4)$$

The anisotropic growth of the particles in the presence of thiourea can be attributed to the self-assembly of sheet-like structures to well-ordered and oriented hierarchical spherical flower-like architectures formed as a result of longer hydrothermal duration (Figure 2c). The average size of the spherical CuS-flower architectures is found to be ∼2 μm. A few sheet-like structures are also observed, which may be due to breaking of the flowers to individual sheets during high ultrasonication for dispersion of the sample. A magnified and high-resolution image of a single flower architecture has been shown in Figure 2d, which calculates the average sheet thickness to be ∼100 nm. It can be visualized that the spherical flower structure and the sheets forming the flower architecture is very consistent and well-distributed, irrespective of the formation of any other morphology. Conclusively, all synthesized CuS powders using different sulfur sources undergo a similar chemical reaction and morphology formation mechanism. It is the release rate of S^{2-} ions under hydrothermal condition that presides over the morphological changes in the metal sulfides.[9]

From the above elucidation, it can be said that immediate nuclei formation followed by anisotropic growth due to high release rate of S^{2-} ions forms sheet-assembled one-dimensional structures. The concentration of S^{2-} is lower but prolonged duration under high pressure changes the morphology. On the basis of the morphology obtained for CuS powders using thioacetamide and thiourea, it can be said that the release of S^{2-} from thiourea is faster whereas thioacetamide dissociation to S^{2-} is slower. As an outcome, CuS nuclei could not grow in an oriented manner in thioacetamide as it did in the presence of a thiourea-based precursor. A graphic representation of the formation of different morphology CuS microstructures with different sulfur sources has been shown in Figure 2e.

For a photocatalyst to be a good candidate, a large surface area along with hierarchical cavities is required. For enhanced photocatalytic activity, the photocatalyst should have higher specific surface area that serves as an important factor because

of the more active catalytic sites being provided for the photochemical reaction. An adsorption−desorption isotherm (nitrogen) has been constructed from the Brunauer−Emmett−Teller (BET) surface area measurement and is depicted in Figure 3a−c for CuS-ST, CuS-TA, and CuS-TU powders, respectively. The isotherms presented in Figure 3a,b can be categorized as type III, which suggests weak interaction between the adsorbate and the adsorbent. There is no observation of the adsorption−desorption hysteresis loop in the isotherm that rules out the mesoporous behavior of the synthesized CuS-ST and CuS-TA powders. However, the isotherm indicated a multilayer gas adsorption, and the specific BET surface areas measured are 5.2 and 6.6 m^2/g for CuS-ST and CuS-TA, respectively. High surface area for CuS-TA in comparison with CuS-ST could be due to the low particle size in CuS-TA than CuS-ST, as observed from FESEM images. There is a significant hysteresis loop in Figure 3c that can be categorized as type IV, which implies the presence of mesopores in the flower structure. The mesoporosity can be attributed to the space between the intercrossed sheets forming flower architectures. The BET surface area of the spherical CuS-flowers (CuS-TU) is measured to be 15.3 m^2/g, with the flower having a pore volume of 6.43×10^{-2} cm^3/g and a pore diameter of 5.8 nm. It is the highest measured surface area among the synthesized photocatalysts, which is due to spherical hierarchical existence of flowers and open cavities in the structure. Thus, it can be attributed that the spherical flower structure obtained in CuS-TU should be a promising photocatalytic candidate for degradation of organic pollutants in comparison with other photocatalysts.

Figure 4a,b shows the typical TEM images of the CuS powders synthesized by thiourea as CuS-TU exhibited high degradation of 4-CP in the presence of visible light irradiation. The TEM image of a single spherical flower architecture is shown in Figure 4a. The average size of the spherical flower is found to be ∼2.3 μm. The observation from the TEM image agrees well with the morphology determined from the FESEM image. The flower edges show the stack-layered orientation of many CuS sheets. Figure 4b depicts the high-resolution
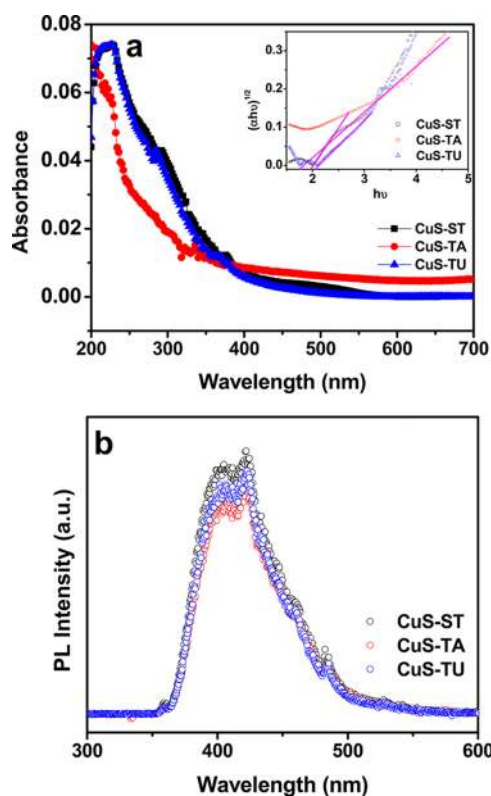
Figure 4. (a) TEM and (b) HRTEM image (inset represents the SAED pattern) of CuS-TU.

Figure 5. (a) UV−vis diffuse reflectance of CuS microstructures (inset represents the Tauc plot) and (b) PL studies of CuS microstructures.

transmission electron microscopy (HRTEM) image of the individual sheet stacked to form the flower architecture. The image shows two well-resolved 2D lattice fringes of 0.33 and 0.19 nm that correlate well with the *d*-spacing of (100) and (110) lattice planes of the as-synthesized hexagonal CuS, respectively. The lattice fringe calculation has been carried out using digital micrograph software. The inset of Figure 4b presents the selected area electron diffraction (SAED) pattern, which shows a highly ordered array of a hexagonal spot, which confirms the formation of hexagonal CuS. The strong and intense spots in the SAED pattern are also indicative of the single crystallinity of each CuS sheet. Thus, it can be concluded that the single crystal CuS sheet forming spherical flower architectures has crystallographic orientation along the (110) plane as predicted from the XRD analysis.

The ultraviolet−visible (UV−vis) absorption spectra of all synthesized CuS structures have been recorded and shown in Figure 5a. All of the absorption spectra show broad feature in the wavelength range from 330 to 600 nm, which can be ascribed to the excitonic absorption from the covellite CuS compound. The UV−vis absorption of CuS-TU and CuS-ST are near similar with a slight shift in absorption from lower to higher wavelength as observed for CuS-ST. This visible light shift with a broad absorption between 400 and 550 nm could be attributed to Cu_2S, which does not have any clear absorption edge, but it extends from the UV to visible region. The mere presence of Cu_2S in the CuS system introduces an impurity level band structure that is responsible for shifting the absorption toward the visible region.[37]

However, the absorption by CuS-TA is blue-shifted because of the quantum confinement effect. The optical energy band gaps (E_g) are determined from their optical spectra by extrapolating the linear region of the band gap plot of $(\alpha h\nu)^2$ versus $h\nu$, which is the photon energy, where α is the corresponding absorption, h is the Planck's constant, and ν is the frequency.[31,38] The estimated band gap values of CuS structures synthesized with sodium thiosulphate, thioacetamide, and thiourea are 1.95, 1.85, and 2.16 eV, respectively. The obtained values are in the range of the band gap values reported by other researchers.[31,39] The results suggest that despite the presence of Cu_2S in CuS-ST, there is no significant difference in the calculated band gap, and thus, the photoactivity of these catalysts will depend on other physicochemical factors.

To identify the photoconductivity and its response, photoluminescence (PL) of CuS powders is of interest. The PL spectra of CuS-ST, CuS-TA, and CuS-TU powders are shown in Figure 5b. For excitation wavelength of 350 nm, a broad intense emission peak at 435 nm is observed along with few

weak peaks in the range between 475 and 550 nm.[40] The nature of the emission spectra and its intensity depends on the inherent morphology and its subsequent property. Although the variation in PL intensity could be attributed to the size effect or surface oxygen vacancy and defects owing to dimensional changes,[41] the peak positions remain unaltered in the present case. Among the three powders synthesized, the intensity of CuS-TA is lower in comparison with both CuS-ST and CuS-TU that suggests that the high photocatalytic activity should be observed for CuS-TA, which is supported by its lower band gap energy calculated from UV−vis diffuse reflectance spectroscopy (DRS). The lowest activity should be observed for CuS-ST as it has the highest PL intensity, which corresponds to the high recombination rate of the electron and hole pair. The formation of Cu_2S in CuS-ST is not carried out under controlled conditions, and no optimization has been made with regard to the concentration of Cu_2S in CuS-ST. Therefore, it can be presumed that the highest PL intensity results from the recombination at the grain boundary centers of Cu_2S particles.[42] Thus, the decrease in the photocatalytic activity using CuS-ST can be anticipated.

X-ray photoelectron spectroscopy (XPS) of CuS-TU powder was carried out to confirm the purity, composition, and valence states of the products obtained as CuS-TU showed the highest photocatalytic activity among the three catalysts. The wide spectrum as shown in Figure 6a indicates the presence of Cu and S along with the presence of other elements such as C and O. The presence of C and O elements is probably due to the exposure to atmosphere on the surface of the powder. The high-resolution spectrum of C 1s (Figure 6b) shows three distinct peaks due to adventitious carbon species at 284.7, 286.2, and 288.1 eV that corresponds to the C−C and C−O−
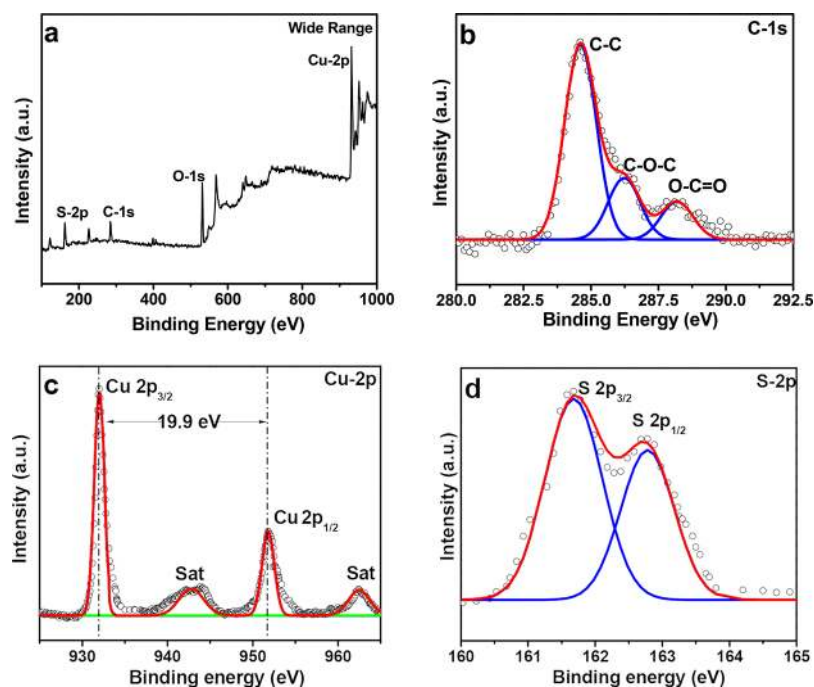
Figure 6. XPS spectra of (a) CuS wide survey scan, (b) C 1s, (c) Cu 2p, and (d) S 2p.
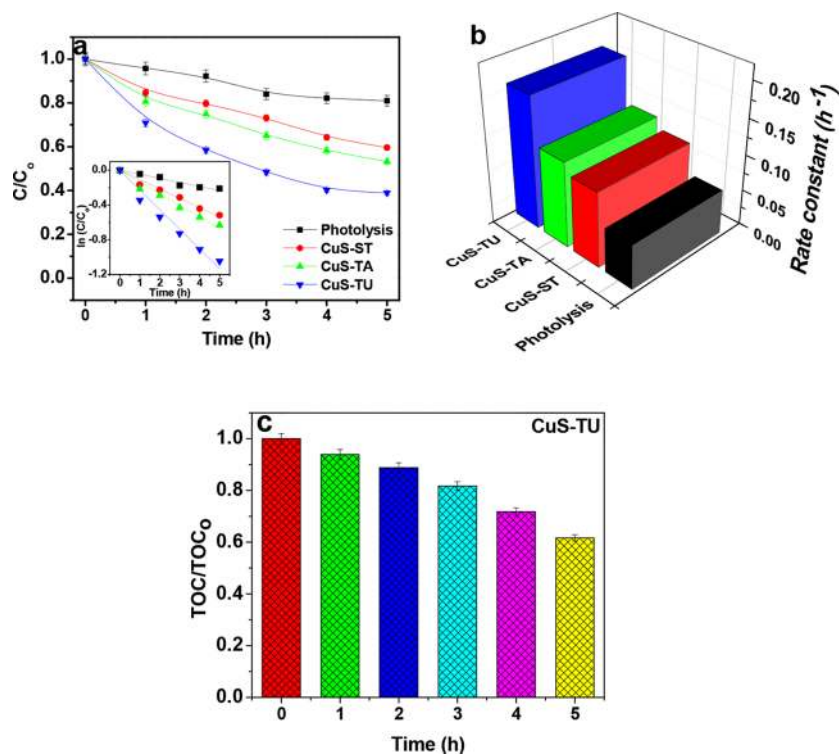

Figure 7. Photocatalysis of 4-CP (a) degradation profile (inset presents the kinetic profile); (b) plot of kinetic rate constants of different CuS microstructures; and (c) total organic carbon (TOC) profile vs time for the CuS-TU photocatalyst. (Parameter constants: catalyst loading—50 mg, initial concentration of 4-CP—100 ppm, temperature—25 ± 2 °C, and visible light intensity—49 700 lux).

C/C−OH formation and O−C═O bonds, respectively. A correction to the binding energy (BE) has been made using the value of 284.8 eV for the observed C 1s charging. The high-resolution XPS of Cu 2p as presented in Figure 6c shows two strong peaks at 931.9 and 951.8 eV, which is consistent with the literature data of Cu $2p_{3/2}$ and Cu $2p_{1/2}$, respectively.[43] These peaks can be attributed to the Cu^{2+} state in CuS structures.

Literature reports the difference between these states to be 20 eV; however, in our case, it is 19.9 eV, which is nearly the same in accordance with the reported value. Two satellite peaks at 942.9 and 963.4 eV have been observed, which correspond to the paramagnetic chemical state of Cu^{2+}. The high-resolution survey of the S 2p region (Figure 6d) shows the presence of two peaks at BE values of 161.7 and 162.7 eV, which can be

4014
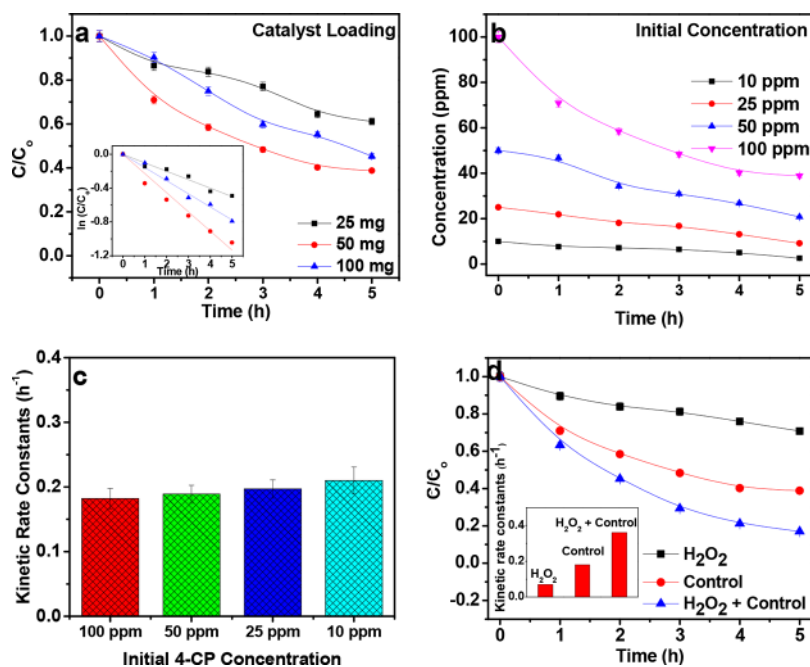
Figure 8. Photocatalysis of 4-CP as an effect of (a) catalyst loading (inset presents the kinetic profile); (b) initial 4-CP concentration; (c) plot of kinetic rate constants vs initial 4-CP concentration; and (d) effect of H_2O_2 oxidizer (inset represents the kinetic rate constants) (parameter constants: chosen catalyst—CuS-TU, initial concentration of 4-CP—100 ppm, temp.—25 $\pm$ 2 °C, and visible light intensity—49 700 lux).

attributed to the S $2p_{3/2}$ and S $2p_{1/2}$ states, respectively.[44] The above data suggest the presence of both the oxidation states of Cu and S in the CuS system.

2.2. Photochemical Degradation of 4-CP. The photocatalytic degradation performances of different CuS samples were evaluated under visible light irradiation for a typical colorless nondye organic contaminant, namely, 4-CP. Figure 7a presents the degradation profile for time-resolved degradation of 4-CP. The degradation profile has been plotted as time (t in h) versus C/C_o, where, C_o is the initial concentration of 4-CP and C is the concentration of 4-CP at time t. The photolytic degradation of 4-CP in the presence of light without the CuS catalyst shows that only ~20% degradation takes place in presence of the visible light (depicted as photolysis in the figure). Prior to each of the photocatalytic degradation, adsorption−desorption equilibrium is achieved, and the concentration of 4-CP after adsorption is considered as initial absorbance of 4-CP. Among the three different CuS structures, a high photocatalytic degradation of ~62% is achieved using CuS-TU after 5 h. A comparatively lower degradation is observed using CuS-TA with a degradation of only ~40%, which is significantly lower than CuS-TU. On the other hand, Cu_2S impurity containing CuS-ST showed only ~25% degradation of 4-CP. The lowest degradation by CuS-ST was also predicted by the PL studies owing to the probable recombination taking place at the grain boundaries of Cu_2S particles in excess.[45]

Upon comparing the degradation efficiencies, it can be said that the high surface area, crystal structure, and also morphology of the CuS structure play an important role in the degradation of 4-CP. Thus, it can be noted that the open flower-like architectures of CuS-TU provided more active catalytic sites than CuS-TA. This increase in activity can also be attributed to the high energy surfaces that have large density of low-coordinated atoms situated on steps and kinks with high reactivity. These favor the fast ionic transfer between the surface and the interior. As known from the XRD and HRTEM data, the crystallographic growth takes place along the (110) plane. The (110) plane is known to have high surface energy that provides the active sites for the photochemical reaction. However, this plane is supposed to be more exposed in spherical CuS-flowers, facilitating high reactivity between active species and adsorbed molecules on the surface.

The degradation data are fitted by a pseudo first-order kinetic equation and represented as ln C/C_o versus time (inset of Figure 7a), which demonstrates that the photocatalytic activities follow the kinetics well. Figure 7b presents the kinetic rate constant plots of different CuS structures. The CuS-TU showed the highest rate constant of 0.18 h^{-1}, which is about ~1.5 and ~2 times that of the kinetic rate constants of CuS-TA (0.12 h^{-1}) and CuS-ST (0.10 h^{-1}), respectively. Because CuS-TU catalyst showed better activity than other existing catalysts, all further experiments were carried out with CuS-TU as the catalyst. Furthermore, TOC was determined to understand the mineralization of 4-CP under visible light using CuS-TU photocatalyst. Because 4-CP is a colorless compound, TOC of the solution obtained at regular photochemical intervals was evaluated as shown in Figure 7c. It can be clearly observed from the figure that the TOC has decreased near to 40% after visible light irradiation for 5 h using CuS-TU catalyst. Thus, the photochemical process is not just mere degradation of 4-CP into organic carbon byproducts but also mineralization that takes place via conversion into carbon dioxide that escapes the liquid. In addition, parametric studies such as catalyst loading and initial concentration of contaminants have been carried out for the reactions with CuS-TU catalyst.

To determine the optimal catalyst amount, various dosages of CuS-TU catalyst (25, 50, and 100 mg) were mixed with 4-CP having a constant initial concentration (100 ppm). Figure 8a presents the degradation profile of 4-CP as an effect of catalyst loading. From the figure, it can be observed that when the catalyst is reduced to half (25 mg) and doubled (100 mg)
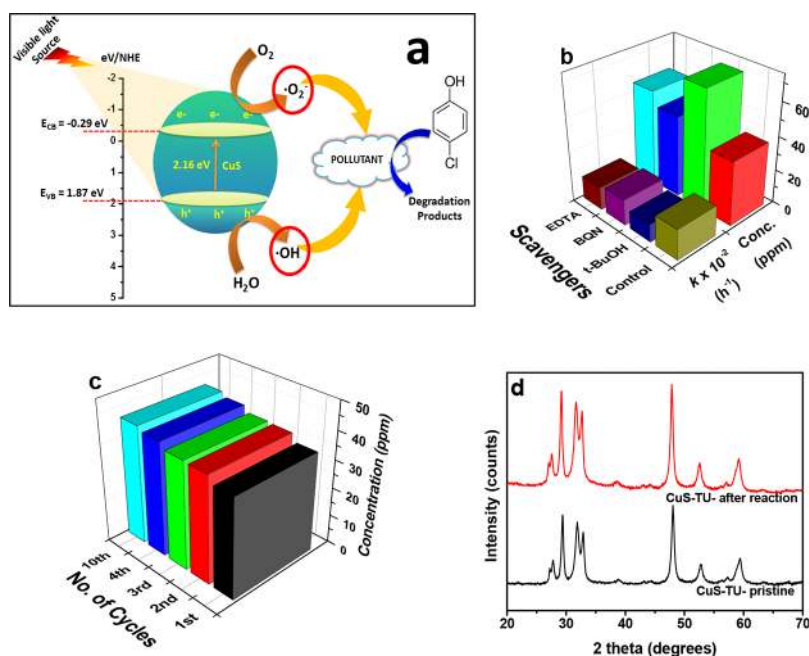
Figure 9. (a) Schematic of photocatalytic mechanism using CuS-TU catalyst; (b) plot of rate constants and concentration vs scavengers; (c) reusability of CuS-TU photocatalyst; and (d) XRD of CuS-TU (before and after the reaction).

from 50 mg in 50 mL of 100 ppm 4-CP solution, the degradation of 4-CP also reduces significantly to ~35 and ~50%, respectively. Increasing the catalyst loading from 25 to 50 mg increases the photocatalytic degradation, but doubling the catalyst concentration to 100 mg from 50 mg decreases the catalytic activity by ~12%. This decrement could be attributed to the solution turbidity that does not allow the light to fall on particles and also segregation of particles become difficult in the solution.[4,46] The inset of Figure 8a demonstrates the kinetic profile of the reaction. The figure shows that the reaction follows the pseudo first-order kinetics well. The kinetic rate constants are 0.09, 0.18, and 0.15 h^{-1} for 25, 50, and 100 mg catalyst loading, respectively. The above data depict that the rate is almost halved when the catalyst loading is half of the optimal condition, that is, 50 mg loading, whereas when the loading is doubled the rate is reduced to 1.2 times. This study suggests that with catalyst loading of 50 mg, the photo-degradation is highest; therefore, 50 mg loading is used for further parametric experiments.

The effect of varying the initial concentration of 4-CP on its photodegradation using CuS-TU catalyst has been shown in Figure 8b. A complete degradation is observed with lowest concentration of 4-CP, that is, 10 ppm. However, the 4-CP concentration of 25, 50, and 100 ppm is photocatalytically reduced to 9.7 ppm (~60% degradation), 20.7 ppm (~59% degradation), and 38 ppm (~62% degradation) concentrations, respectively. A better outlook to the reaction processes could be understood from the kinetic rate constants of the reactions, which has been calculated using the first-order kinetic equation. Figure 8c shows the plot of calculated kinetic rate constants at different initial concentrations of 4-CP. The first-order rate constant is almost constant irrespective of the initial concentration of 10 ppm (0.21 h^{-1}), 25 ppm (0.197 h^{-1}), 50 ppm (0.189 h^{-1}), and 100 ppm (0.182 h^{-1}). For higher concentration of 4-CP, that is, 100 ppm, experiments have been carried out in the presence of hydrogen peroxide as the
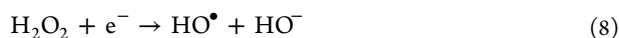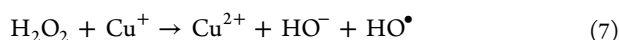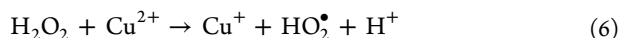
concentration of oxidant increases the rate of degradation significantly.

Figure 8d compares the photocatalytic degradation of 100 ppm of 4-CP with the influence of visible light in three different conditions: (i) in the presence of H_2O_2 (without catalyst, designated as H_2O_2); (ii) in the presence of catalyst (without H_2O_2, designated as control); and (iii) in the presence of both H_2O_2 and catalyst (designated as H_2O_2 + control). The concentration of hydrogen peroxide taken is 5 mM, which is kept constant in both the photochemical reactions except in control experiments. The degradation of 4-CP in the presence of H_2O_2 solution under irradiation is via photolysis of H_2O_2, that is, through hemolytic cleavage of H_2O_2 producing $HO^{\bullet}$ radicals, which contributes to the photochemical reaction (eq 5). The degradation observed in the presence of H_2O_2 is nearly 30%, which is 10% higher than the photolysis (20%). This phenomenon indicates that the production of hydroxyl radicals for the degradation of 4-CP in the presence of H_2O_2 is very slow. However, in comparison with control experiment that exhibits 62% degradation, the degradation of 4-CP is enhanced by ~21% in the presence of H_2O_2 with control (~83% degradation). The inset of Figure 8d shows the rate constants of the photochemical reactions, which evidently indicate that the rate of the reaction increases significantly in the presence of an oxidizer which is 0.36 h^{-1}. There is a twofold increase in the rate when compared to control (0.18 h^{-1}). Although the rate is increased, complete degradation of 4-CP is still not achieved with 5 mM H_2O_2 that advocates may be a higher concentration of the oxidizer or prolonged reaction time that can oxidize the pollutant completely. Apart from the photolytic production of $HO^{\bullet}$ radicals that contribute to the photochemical reaction, Cu^{2+} in CuS-TU can also react with the oxidizer to produce hydroxyl radicals and carry out the reaction as given in eqs 6 and 7.

Additionally, H_2O_2 also accepts the photogenerated electron for CuS that inhibits the electron−hole pair recombination and also facilitates additional $HO^{\bullet}$ radicals as shown in eq 8. Thus,

the probable involved chemical reactions in the presence of the oxidizer are given as follows[47]

$$H_2O_2 \rightarrow 2HO^\bullet \tag{5}$$

$$H_2O_2 + Cu^{2+} \rightarrow Cu^+ + HO_2^\bullet + H^+ \tag{6}$$

$$H_2O_2 + Cu^+ \rightarrow Cu^{2+} + HO^- + HO^\bullet \tag{7}$$

$$H_2O_2 + e^- \rightarrow HO^\bullet + HO^- \tag{8}$$

In a photochemical reaction, the photoinduced electrons and holes are generated as a result of excitation of electrons from the valence band (VB) to the conduction band (CB) upon visible light illumination. The level of the VB and the CB of CuS has been calculated using the given relation[48]
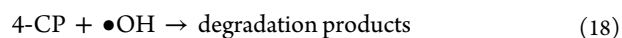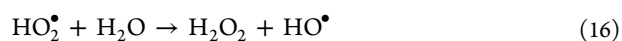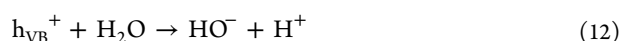
$$E_{VB} = X - E_e + 0.5E_g \tag{9}$$

$$E_{CB} = E_{VB} - E_g \tag{10}$$

In eqs 9 and 10, E_{VB} is the VB potential edge, X is the electronegativity of the semiconductor material, E_e is the free electron energy on the hydrogen scale ($\sim$4.5 eV), E_g is the energy band gap of the prepared CuS-TU catalyst, and E_{CB} is the CB potential edge. The electronegativity of the CuS material can be obtained from the arithmetic mean of the electron affinity and the first ionization energy of the constituent atoms, as reported in literature to be 5.29 eV. The calculated CB and VB potentials of CuS-TU catalyst are −0.29 and 1.87 eV versus normal hydrogen electrode, respectively. A corresponding band diagram of CuS-TU has been plotted and shown in Figure 9a, which indicates that the photogenerated electron and hole can stimulate both the adsorbed oxygen and water molecules on the catalyst surface to produce reactive oxygen species such as $O_2^{-\bullet}$ (superoxide anion) and $\bullet OH$ (hydroxyl) radicals, respectively. These reactive oxygen species can initialize the catalytic reactions by typical reaction pathways on the catalyst surface to degrade the organic molecules.[6,49]

To better understand the possible mechanism for the degradation of 4-CP via these reactive species, experiments have been carried out in the presence of the scavengers to determine the contribution of species in the photochemical reaction without the presence of the oxidizer H_2O_2. The effect of different scavenging additives such as ethylenediamine tetraacetic acid (h^+ scavenger, EDTA), benzoquinone ($\bullet O_2^-$ scavenger, BQN), and tert-butylalcohol ($\bullet OH$ scavenger, t-BuOH) on the photochemical reaction is studied with 1 mM of the scavenging agent in the control solution. Figure 9b presents the concentration of 4-CP and rate constants of the photochemical reaction carried out in presence of the scavengers. A careful observation reveals that a significant decrease in reaction rate is found in the presence of the hydroxyl radical scavenger, that is, t-BuOH ($\sim$10 × 10^{-2} h^{-1}) in comparison with the reaction rate of the control experiment ($\sim$21 × 10^{-2} h^{-1}), and the concentration after the reaction was near to 72 ppm. However, there is not much difference between the rates of reaction of t-BuOH ($\sim$10 × 10^{-2} h^{-1}) and EDTA ($\sim$13 × 10^{-2} h^{-1}) but a significant difference in concentration ($\sim$16 ppm) after the reaction signifies the efficient scavenging property of t-BuOH than EDTA, which showed a moderate decrease in the efficiency of catalytic degradation. This suggests that the photogenerated hole in the reaction also have partial contribution in degradation, which is

governed by hydroxyl radicals produced as a result of chain reactions with holes. The high reaction rate of BQN ($\sim$15 × 10^{-2} h^{-1}) could be attributed to the disproportionation of the superoxide radical to form hydroxyl radicals that contributes to the redox reaction degrading 4-CP. The rate of BQN is 1.45 times greater than the rate of reaction of t-BuOH. The scavenging experiments concluded that the hydroxyl radicals are the prime reactive oxygen species that are involved in the photodegradation of 4-CP. Literature reports that the degradation pathways for 4-CP through hydroxyl radicals are via production of hydroquinone and hydroxyhydroquinone as reaction intermediates.[50,51] Considering the materials perspective, based on the above observations, a photocatalytic mechanism has been deduced for the degradation of 4-CP using CuS-TU catalyst in the absence of the oxidizer. The catalytic degradation using CuS-TU catalyst is given by the following equations[19]

$$CuS + h\nu \rightarrow e_{CB}^- + h_{VB}^+ \tag{11}$$

$$h_{VB}^+ + H_2O \rightarrow HO^- + H^+ \tag{12}$$

$$h_{VB}^+ + OH^- \rightarrow HO^\bullet \tag{13}$$

$$e_{CB}^- + O_2 \rightarrow O_2^{\bullet -} \tag{14}$$

$$O_2^{\bullet -} + H^+ \rightarrow HO_2^\bullet \tag{15}$$

$$HO_2^\bullet + H_2O \rightarrow H_2O_2 + HO^\bullet \tag{16}$$

$$H_2O_2 \rightarrow 2HO^\bullet \tag{17}$$

$$4\text{-CP} + \bullet OH \rightarrow \text{degradation products} \tag{18}$$

For practical application of the heterogeneous catalyst, recyclability and stability of the catalyst is an important factor. Thus, recyclability of the CuS-TU catalyst has been carried out to understand the reactivity of the samples with consecutive reuse, till 10 cycles (Figure 9c). After each of the photochemical experiments, the catalyst was separated from the 4-CP solution via centrifugation, washed with water and ethanol, followed by drying at 60 °C for 12 h in a hot air oven. The dried catalyst was then reused for the second experiment. However, it can be noticed that with each consecutive recycle the concentration of 4-CP increases, which suggests that first run has the highest degradation efficiency that decreases with increasing cycles. This decrement could be attributed to the loss of catalyst during the recycling process, which reduces the active sites, thereby rendering less activity compared with the pristine powder. There is a difference of only 5% in concentration between the 1st and the 10th run, which indicates that the catalyst is stable and recyclable. To further understand the stability of the catalyst, the physicochemical characteristics such as phase and surface area of the catalyst after the reaction were studied. Figure 9d represents the XRD pattern of the CuS-TU catalyst before and after the reaction (CuS-TU catalyst obtained after the 10th cycle). There is no significant difference in the XRD pattern of CuS-TU after the reaction as they match well with the pristine synthesized CuS-TU powder. However, a negligible difference in the surface area of the powder is observed after the reaction. The surface area of CuS-TU catalyst after 10 consecutive cycles exhibited a surface area of $\sim$14 m^2/g, which is lower than the surface area of the pristine powder. Thus, it can be said that with the lowering of

Table 1. Comparison of Photocatalytic Performance of Recently Reported Hierarchical CuS Structures and This Work

CuS	synthesis route & chemicals	surface area (m^2/g)	pollutants concentration	light source	degradation in time	refs
ball-flower-shaped CuS	hydrothermal & $CuCl_2$, thiourea, polyvinylpyrrolidone	78.6	rhodamine B (2×10^{-5} M)	UV light	100% in 60 min	11
hierarchical CuS	solvothermal & $Cu(NO_3)_2$, thiourea, ethylene glycol		methylene blue (20 ppm)	natural light	90% in 90 min	52
hierarchical flower-CuS hollow nanospheres	solvothermal & $Cu(CH_3COO)_2 \cdot H_2O$, thiourea, glacial acetic acid, methanol	56	rhodamine B (10 ppm)	150 W Xe-lamp	100% in 40 min	53
			2,4-dichlorophenol (10 ppm)		100% in 240 min	
Cu@CuS cubes	yolk−shell (shell sulfidation & core disproportionation) $CuSO_4 \cdot 5H_2O$, $Na_2S \cdot 9H_2O$		methylene blue (2×10^{-2} M)	300 W Xe-lamp	100% in 200 min	54
CuS−Cu_2S nanoparticles	chemical reduction & $Cu(CH_3COO)_2 \cdot H2O$ ethylene glycol, thiourea		methylene blue (1×10^{-5} M)	direct sunlight	61% in 150 min	14
			malachite green		90% in 80 min	
			methyl orange		9% in 200 min	
			rhodamine B		70% in 80 min	
CuS−Cu_2S elongated structure	hydrothermal & $Cu(NO_3)_2$, sodium thiosulphate	5.2	4-CP (100 ppm)	400 W metal halide lamp	35% in 5 h	this work
CuS particles	$Cu(NO_3)_2$, thioacetamide	6.6			50% in 5 h	
spherical CuS-flowers	$Cu(NO_3)_2$, thiourea	15.3			83% in 5 h	

the surface area, the active surface site also reduces, and therefore, the photocatalytic activity drops in comparison.

In the recent past, CuS ball flowers were synthesized hydrothermally using copper chloride and thiourea in the presence of poly(vinylpyrrolidone) as a surfactant. Ball-flower-shaped CuS was tested for photocatalytic degradation of rhodamine B (RhB) under UV light irradiation, and complete degradation was achieved in 60 min.[11] Another research by Li et al. illustrated a solvothermal route to prepare hierarchical CuS nanostructures using thiourea, and 90% degradation of methylene blue (20 ppm) under visible light was achieved with the assistance of the oxidizer (H_2O_2).[52] The latter reported that the degradation value is similar to the value reported in the present work, but the difference remains in the type of pollutant. It is not appropriate to compare the catalytic results unless the conditions of experiments that are carried out are similar. However, a comparative report consisting of work on different organic pollutant degradation using CuS structures with specific parameters (CuS synthesis route, chemicals used, morphology, surface area, pollutants, concentration, illumination source, degradation in time, and others) has been tabulated (Table 1). As can be observed from the tabulated data, in most of the cases, pollutant concentration is very low and UV light/sunlight has been used, which completely degrades the organic pollutant, mainly dyes. The presence of sunlight degrades the dye completely but as UV light is present in sunlight, it is difficult to differentiate the effect of visible light and UV light. Therefore, the visible light response of CuS structures is necessary and has been accomplished in this study.

3. CONCLUSIONS

Hierarchical CuS microstructures were successfully synthesized by the hydrothermal route using a common base precursor and different sulfur sources at 150 °C for 24 h. The physicochemical analysis of the CuS powders suggested the formation of pure hexagonal phase with variant morphologies. The study reveals that the release rate of S^{2-} ions from the complex plays a crucial role governing the nucleation and growth process under elevated temperature to form different hierarchical structures.

The synthesized CuS photocatalysts were tested for their photocatalytic assessment toward 4-CP under visible light. The results showed that thiourea-assisted flower-like CuS architectures exhibited the highest degradation efficiency and depended on the surface area of the catalyst as well. The hydroxyl radical species were observed to have the crucial contribution to the degradation of 4-CP, and the catalyst showed an efficient recyclability and reusability.

4. EXPERIMENTAL SECTION

4.1. Preparation of CuS Photocatalyst. The CuS photocatalyst was prepared by a rapid and one-step hydrothermal method. In a typical synthesis, 40 mL of aqueous solution of $Cu(NO_3)_2 \cdot 3H_2O$ was prepared by dissolving 1 mmol of the compound. To the above solution, 2.5 mmol $Na_2S_2O_3$ was added under stirring to ensure complete dissolution of reactants. The prepared solution was taken as the precursor for the hydrothermal reaction. The precursor solution was then transferred to a 50 mL Teflon-lined stainless steel autoclave followed by tight sealing of the autoclave. The reaction vessel was kept inside of the preheated furnace at 150 °C for 24 h duration. After the stipulated duration, the furnace was switched off and the reaction vessel was allowed to cool down naturally to the room temperature. The black precipitated solution was thoroughly washed with distilled water and absolute ethanol. The precipitate obtained after washing was dried in a crystallization dish at 70 °C for 5 h. A similar process was repeated using C_2H_5NS and CH_4N_2S as other sulfur sources. Finally, three different powders synthesized using sodium thiosulphate, thioacetamide, and thiourea were named CuS-ST, CuS-TA, and CuS-TU, respectively, in which the state of sulfur in all three sources were the same.

4.2. Catalyst Characterizations. The crystal phases of the prepared photocatalysts were recorded by powder XRD measurements on a Rigaku diffractometer with Cu K_α radiation (λ = 0.15406 nm). Specific surface area (BET) of the photocatalysts were obtained from nitrogen adsorption−desorption isotherms (BELSORP). Prior to the surface area and isotherm determination, regeneration of photocatalyst at

150 °C for 90 min was carried to remove the moisture. Raman measurements of all photocatalysts were carried out in backscattering geometry with a triple-grating spectrometer equipped with a cooled charge-coupled device detector. The 532 nm line of an Ar^+/Kr^+ mixed-gas laser was used for excitation. The study of the morphology of the photocatalysts was observed through scanning electron microscopy (SEM) ULTRA 55-FESEM, Carl Zeiss. The sample preparation for SEM was carried through dispersion of catalyst in absolute ethanol and ultrasonication of dispersion for 30 min. Silicon wafers were used as the dispersion substrate, and the dispersion was drop-casted onto it followed by drying at 90 °C in hot air oven. The prepared SEM samples were desiccated under vacuum for 24 h and sputtered with gold using Quorum sputtering. High-resolution study of the optimized photocatalyst was carried out using a transmission electron microscope (JEOL JEM-2100 system). Transmission electron microscopy (TEM) sample preparation is similar to that of the FESEM except for the dispersing solvent, which was isopropanol and the drop-casting substrate, which was Cugrid in the TEM measurement. UV–vis diffuse reflectance spectra of all photocatalysts were carried in a PerkinElmer, Lambda 35 UV vis spectrophotometer in the wavelength window of 200 to 700 nm using $BaSO_4$ as a reference. PL measurements of the photocatalysts were carried using a Hitachi F-4500 spectrofluorimeter in the wavelength range from 200 to 600 nm. The X-ray photoelectron spectroscopy (XPS) measurement of the optimized catalyst was performed on a Axis Ultra X-ray photoelectron spectrometer. The BE was referenced to C 1s line at 284.8 eV from the adventitious carbon.

4.3. Photochemical Experiments. The photocatalytic performance of the synthesized CuS photocatalysts was evaluated by the degradation of 4-CP under visible light irradiation. The visible light experiments were carried by using a 400 W metal halide lamp obtained from Philips, India, with light intensity ~49 700 lux. The metal halide lamp was jacketed with a quartz tube, and the tube was in continuous supply of water using a chiller (maintained at 20 °C) to ensure reaction under room temperature. The reaction solution to undergo catalytic reaction was placed in a quartz beaker. Prior to the photochemical reaction, a standard stock solution of 100 ppm 4-CP was prepared, which was maintained throughout the photocatalytic reaction. For photochemical reaction using different CuS catalysts, the catalyst concentration was kept constant at 1 g/L. Before each of the photochemical experiments, adsorption–desorption equilibrium was attained by keeping the mixed 4-CP-catalyst suspension in dark (in the absence of light). During the catalytic experiments, 2 mL of suspension was taken out at certain time intervals and centrifuged (3000 rpm for 30 min) to separate the catalyst and supernatant. The supernatant was further filtered through doubly stacked 0.22 membrane filters to assure the complete removal of particles, and samples were analyzed using the high-performance liquid chromatography (HPLC) technique. The TOC of the filtered solution obtained after different time intervals of the photochemical reaction using CuS-TU catalyst was also examined with the Shimadzu, TOC V_{CSN} analyzer.

4.4. Sample Analysis. The extent of degradation of 4-CP was determined using the HPLC technique. The HPLC instrument consisted of an isocratic pump (Waters 515 HPLC pump), a Rheodyne injector, C-18 Column, a UV detector (Waters 2487), and a data acquisition system. The mobile phase consisted of 50% water and 50% acetonitrile in volume with 0.1% formic acid. The mobile phase was pumped at the rate of 0.4 mL/min. The filtered samples were injected through the Rheodyne valve with a sample loop of 20 μL, and the UV absorbance at 283 nm was monitored by a UV detector and stored in the digital mode. The chromatograph obtained was converted to concentration units using the calibration carried with pure standard solution of compounds. Additionally, individual experiments in the presence of the oxidizer and trapping agents were also carried to understand the involvement of reactive species. The oxidizer (5 mM) and 1 mM trapping agents were added to the optimized photochemical conditions.

■ AUTHOR INFORMATION

Corresponding Author
*E-mail: giridhar@chemeng.iisc.ernet.in, giridharmadras@gmail.com (G.M.).
ORCID ⬤
Sangeeta Adhikari: 0000-0002-0860-1922
Giridhar Madras: 0000-0003-2211-5055
Notes
The authors declare no competing financial interest.

■ REFERENCES

(1) Wang, J.; Xia, Y.; Zhao, H.; Wang, G.; Xiang, L.; Xu, J.; Komarneni, S. Oxygen defects-mediated Z-scheme charge separation in g-C_3N_4/ZnO photocatalysts for enhanced visible-light degradation of 4-chlorophenol and hydrogen evolution. *Appl. Catal., B* **2017**, *206*, 406−416.

(2) Catrinescu, C.; Arsene, D.; Teodosiu, C. Catalytic wet hydrogen peroxide oxidation of para-chlorophenol over Al/Fe pillared clays (AlFePILCs) prepared from different host clays. *Appl. Catal., B* **2011**, *101*, 451−460.

(3) Barnes, R. J.; Riba, O.; Gardner, M. N.; Scott, T. B.; Jackman, S. A.; Thompson, I. P. Optimization of nano-scale nickel/iron particles for the reduction of high concentration chlorinated aliphatic hydrocarbon solutions. *Chemosphere* **2010**, *79*, 448−454.

(4) Gaya, U. I.; Abdullah, A. H.; Zainal, Z.; Hussein, M. Z. Photocatalytic treatment of 4-chlorophenol in aqueous ZnO suspensions: Intermediates, influence of dosage and inorganic anions. *J. Hazard. Mater.* **2009**, *168*, 57−63.

(5) Andreozzi, R.; Caprio, V.; Insola, A.; Marotta, R. Advanced oxidation processes (AOP) for water purification and recovery. *Catal. Today* **1999**, *53*, 51−59.

(6) Chong, M. N.; Jin, B.; Chow, C. W. K.; Saint, C. Recent developments in photocatalytic water treatment technology: A review. *Water Res.* **2010**, *44*, 2997−3027.

(7) Kalantar-zadeh, K.; Ou, J. Z.; Daeneke, T.; Mitchell, A.; Sasaki, T.; Fuhrer, M. S. Two dimensional and layered transition metal oxides. *Appl. Mater. Today* **2016**, *5*, 73−89.

(8) Shinde, D. V.; Patil, S. A.; Cho, K.; Ahn, D. Y.; Shrestha, N. K.; Mane, R. S.; Lee, J. K.; Han, S.-H. Revisiting Metal Sulfide Semiconductors: A Solution-Based General Protocol for Thin Film Formation, Hall Effect Measurement, and Application Prospects. *Adv. Funct. Mater.* **2015**, *25*, 5739−5747.

(9) Tanveer, M.; Cao, C.; Ali, Z.; Aslam, I.; Idrees, F.; Khan, W. S.; But, F. K.; Tahir, M.; Mahmood, N. Template free synthesis of CuS nanosheet-based hierarchical microspheres: an efficient natural light driven photocatalyst. *CrystEngComm* **2014**, *16*, 5290−5300.

(10) Zoolfakar, A. S.; Rani, R. A.; Morfa, A. J.; O'Mullane, A. P.; Kalantar-zadeh, K. Nanostructured copper oxide semiconductors: a perspective on materials, synthesis methods and applications. *J. Mater. Chem. C* **2014**, *2*, 5247−5270.

(11) Cheng, Z.; Wang, S.; Wang, Q.; Geng, B. A facile solution chemical route to self-assembly of CuS ball-flowers and their application as an efficient photocatalyst. *CrystEngComm* **2010**, *12*, 144−149.

(12) Zhu, T.; Xia, B.; Zhou, L.; Lou, X. W. Arrays of ultrafine CuS nanoneedles supported on a CNT backbone for application in supercapacitors. *J. Mater. Chem.* **2012**, *22*, 7851−7855.

(13) He, W.; Jia, H.; Li, X.; Lei, Y.; Li, J.; Zhao, H.; Mi, L.; Zhang, L.; Zheng, Z. Understanding the formation of CuS concave super-structures with peroxidase-like activity. *Nanoscale* **2012**, *4*, 3501−3506.

(14) Shamraiz, U.; Badshah, A.; Hussain, R. A.; Nadeem, M. A.; Saba, S. Surfactant free fabrication of copper sulphide (CuS−Cu₂S) nanoparticles from single source precursor for photocatalytic applications. *J. Saudi Chem. Soc.* **2017**, *21*, 390−398.

(15) Yu, S.; Liu, J.; Zhu, W.; Hu, Z.-T.; Lim, T.-T.; Yan, X. Facile room-temperature synthesis of carboxylated graphene oxide-copper sulfide nanocomposite with high photodegradation and disinfection activities under solar light irradiation. *Sci. Rep.* **2015**, *5*, 16369.

(16) Basu, M.; Sinha, A. K.; Pradhan, M.; Sarkar, S.; Negishi, Y.; Govind; Pal, T. Evolution of Hierarchical Hexagonal Stacked Plates of CuS from Liquid−Liquid Interface and its Photocatalytic Application for Oxidative Degradation of Different Dyes under Indoor Lighting. *Environ. Sci. Technol.* **2010**, *44*, 6313−6318.

(17) Shu, Q. W.; Lan, J.; Gao, M. X.; Wang, J.; Huang, C. Z. Controlled synthesis of CuS caved superstructures and their application to the catalysis of organic dye degradation in the absence of light. *CrystEngComm* **2015**, *17*, 1374−1380.

(18) Nie, G.; Li, Z.; Lu, X.; Lei, J.; Zhang, C.; Wang, C. Fabrication of polyacrylonitrile/CuS composite nanofibers and their recycled application in catalysis for dye degradation. *Appl. Surf. Sci.* **2013**, *284*, 595−600.

(19) Xu, W.; Zhu, S.; Liang, Y.; Li, Z.; Cui, Z.; Yang, X.; Inoue, A. Nanoporous CuS with excellent photocatalytic property. *Sci. Rep.* **2015**, *5*, 18125.

(20) Zhuang, T.-T.; Fan, F.-J.; Gong, M.; Yu, S.-H. Cu1.94S nanocrystal seed mediated solution-phase growth of unique Cu₂S−PbS heteronanostructures. *Chem. Commun.* **2012**, *48*, 9762−9764.

(21) Wei, T.; Liu, Y.; Dong, W.; Zhang, Y.; Huang, C.; Sun, Y.; Chen, X.; Dai, N. Surface-Dependent Localized Surface Plasmon Resonances in CuS Nanodisks. *ACS Appl. Mater. Interfaces* **2013**, *5*, 10473−10477.

(22) Fu, W.; Liu, M.; Xue, F.; Wang, X.; Diao, Z.; Guo, L. Facile polyol synthesis of CuS nanocrystals with a hierarchical nanoplate structure and their application for electrocatalysis and photocatalysis. *RSC Adv.* **2016**, *6*, 80361−80367.

(23) Subramanyam, K.; Sreelekha, N.; Reddy, D. A.; Murali, G.; Varma, K. R.; Vijayalakshmi, R. P. Chemical synthesis, structural, optical, magnetic characteristics and enhanced visible light active photocatalysis of Ni doped CuS nanoparticles. *Solid State Sci.* **2017**, *65*, 68−78.

(24) Patil, A. M.; Lokhande, A. C.; Chodankar, N. R.; Shinde, P. A.; Kim, J. H.; Lokhande, C. D. Interior design engineering of CuS architecture alteration with rise in reaction bath temperature for high performance symmetric flexible solid state supercapacitor. *J. Ind. Eng. Chem.* **2017**, *46*, 91−102.

(25) Lu, Y.; Liu, X.; Wang, W.; Cheng, J.; Yan, H.; Tang, C.; Kim, J.-K.; Luo, Y. Hierarchical, porous CuS microspheres integrated with carbon nanotubes for high-performance supercapacitors. *Sci. Rep.* **2015**, *5*, 16584.

(26) Saranya, M.; Santhosh, C.; Ramachandran, R.; Kollu, P.; Saravanan, P.; Vinoba, M.; Jeong, S. K.; Grace, A. N. Hydrothermal

growth of CuS nanostructures and its photocatalytic properties. *Powder Technol.* **2014**, *252*, 25−32.

(27) Liu, B.; Ma, Y.; Zhao, D.; Xu, L.; Liu, F.; Zhou, W.; Guo, L. Effects of morphology and concentration of CuS nanoparticles on alignment and electro-optic properties of nematic liquid crystal. *Nano Res.* **2017**, *10*, 618−625.

(28) Colomban, C.; Kudrik, E. V.; Afanasiev, P.; Sorokin, A. B. Degradation of chlorinated phenols in water in the presence of H₂O₂ and water-soluble μ-nitrido diiron phthalocyanine. *Catal. Today* **2014**, *235*, 14−19.

(29) Gan, T.; Lv, Z.; Sun, J.; Shi, Z.; Liu, Y. Preparation of graphene oxide-wrapped carbon sphere@silver spheres for high performance chlorinated phenols sensor. *J. Hazard. Mater.* **2016**, *302*, 188−197.

(30) Krýsa, J.; Waldner, G.; Měšťánková, H.; Jirkovský, J.; Grabner, G. Photocatalytic degradation of model organic pollutants on an immobilized particulate TiO₂ layer: Roles of adsorption processes and mechanistic complexity. *Appl. Catal., B* **2006**, *64*, 290−301.

(31) Kundu, J.; Pradhan, D. Influence of precursor concentration, surfactant and temperature on the hydrothermal synthesis of CuS: structural, thermal and optical properties. *New J. Chem.* **2013**, *37*, 1470−1478.

(32) Hurma, T.; Kose, S. XRD Raman analysis and optical properties of CuS nanostructured film. *Optik* **2016**, *127*, 6000−6006.

(33) Yeryukov, N. A.; Milekhin, A. G.; Sveshnikova, L. L.; Duda, T. A.; Pokrovsky, L. D.; Gutakovskii, A. K.; Batsanov, S. A.; Rodyakina, E. E.; Latyshev, A. V.; Zahn, D. R. T. Synthesis and Characterization of CuₓS (x = 1−2) Nanocrystals Formed by the Langmuir−Blodgett Technique. *J. Phys. Chem. C* **2014**, *118*, 23409−23414.

(34) Lu, Q.; Gao, F.; Zhao, D. One-Step Synthesis and Assembly of Copper Sulfide Nanoparticles to Nanowires, Nanotubes, and Nano-vesicles by a Simple Organic Amine-Assisted Hydrothermal Process. *Nano Lett.* **2002**, *2*, 725−728.

(35) Saranya, M.; Santhosh, C.; Ramachandran, R.; Grace, A. N. Growth of CuS Nanostructures by Hydrothermal Route and Its Optical Properties. *J. Nanotechnol.* **2014**, *2014*, 1−8.

(36) Bai, L.; Ye, X.; Song, C.; Chen, H.; Cai, B.; Bai, Y.; Xu, C.; Li, Z. The surfactant-free synthesis of hollow CuS nanospheres via clean Cu₂O templates and their catalytic oxidation of dye molecules with H₂O₂. *RSC Adv.* **2016**, *6*, 83885−83889.

(37) Michael, R. J. V.; Theerthagiri, J.; Madhavan, J.; Umapathy, M. J.; Manoharan, P. T. Cu₂S-incorporated ZnS nanocomposites for photocatalytic hydrogen evolution. *RSC Adv.* **2015**, *5*, 30175−30186.

(38) Pradhan, D.; Mohapatra, S. K.; Tymen, S.; Misra, M.; Leung, K. T. Morphology-controlled ZnO nanomaterials for enhanced photo-electrochemical performance. *Mater. Express* **2011**, *1*, 59−67.

(39) Riyaz, S.; Parveen, A.; Azam, A. Microstructural and optical properties of CuS nanoparticles prepared by sol−gel route. *Perspectives Sci.* **2016**, *8*, 632−635.

(40) Wang, X.; Li, Y.; Wang, M.; Li, W.; Chen, M.; Zhao, Y. Synthesis of tunable ZnS−CuS microspheres and visible-light photoactivity for rhodamine B. *New J. Chem.* **2014**, *38*, 4182−4189.

(41) Wang, W.-N.; Widiyastuti, W.; Ogi, T.; Lenggoro, I. W.; Okuyama, K. Correlations between Crystallite/Particle Size and Photoluminescence Properties of Submicrometer Phosphors. *Chem. Mater.* **2007**, *19*, 1723−1730.

(42) Chen, Y.; Qin, Z.; Wang, X.; Guo, X.; Guo, L. Noble-metal-free Cu₂S-modified photocatalysts for enhanced photocatalytic hydrogen production by forming nanoscale p−n junction structure. *RSC Adv.* **2015**, *5*, 18159−18166.

(43) Jin, X.; Li, J.; Chen, G.; Xue, C.; Liu, W.; Zhu, C. Preparation of Cu2ZnSnS4-based thin film solar cells by a combustion method. *Sol. Energy Mater. Sol. Cells* **2016**, *146*, 16−24.

(44) An, L.; Huang, L.; Zhou, P.; Yin, J.; Liu, H.; Xi, P. A Self-Standing High-Performance Hydrogen Evolution Electrode with Nanostructured NiCo₂O₄/CuS Heterostructures. *Adv. Funct. Mater.* **2015**, *25*, 6814−6822.

(45) Wang, B.; An, W.; Liu, L.; Chen, W.; Liang, Y.; Cui, W. Novel Cu₂S quantum dots coupled flower-like BiOBr for efficient photo-

catalytic hydrogen production under visible light. *RSC Adv.* **2015**, *5*, 3224−3231.

(46) Chiou, C.-H.; Wu, C.-Y.; Juang, R.-S. Influence of operating parameters on photocatalytic degradation of phenol in UV/TiO$_2$ process. *Chem. Eng. J.* **2008**, *139*, 322−329.

(47) Yang, J.; Dai, J.; Chen, C.; Zhao, J. Effects of hydroxyl radicals and oxygen species on the 4-chlorophenol degradation by photo-electrocatalytic reactions with TiO$_2$-film electrodes. *J. Photochem. Photobiol., A* **2009**, *208*, 66−77.

(48) Dong, H.; Chen, G.; Sun, J.; Feng, Y.; Li, C.; Xiong, G.; Lv, C. Highly-effective photocatalytic properties and interfacial transfer efficiencies of charge carriers for the novel Ag$_2$CO$_3$/AgX hetero-junctions achieved by surface modification. *Dalton Trans.* **2014**, *43*, 7282−7289.

(49) Mi, L.; Wei, W.; Zheng, Z.; Gao, Y.; Liu, Y.; Chen, W.; Guan, X. Tunable properties induced by ion exchange in multilayer intertwined CuS microflowers with hierarchal structures. *Nanoscale* **2013**, *5*, 6589−6598.

(50) Priya, M. H.; Madras, G. Kinetics of Photocatalytic Degradation of Chlorophenol, Nitrophenol, and Their Mixtures. *Ind. Eng. Chem. Res.* **2006**, *45*, 482−486.

(51) Li, X.; Cubbage, J. W.; Tetzlaff, T. A.; Jenks, W. S. Photocatalytic Degradation of 4-Chlorophenol. 1. The Hydroquinone Pathway. *J. Org. Chem.* **1999**, *64*, 8509−8524.

(52) Li, F.; Wu, J.; Qin, Q.; Li, Z.; Huang, X. Controllable synthesis, optical and photocatalytic properties of CuS nanomaterials with hierarchical structures. *Powder Technol.* **2010**, *198*, 267−274.

(53) Meng, X.; Tian, G.; Chen, Y.; Zhai, R.; Zhou, J.; Shi, Y.; Cao, X.; Zhou, W.; Fu, H. Hierarchical CuS hollow nanospheres and their structure-enhanced visible light photocatalytic properties. *CrystEng-Comm* **2013**, *15*, 5144−5149.

(54) Li, Q.; Wang, F.; Sun, L.; Jiang, Z.; Ye, T.; Chen, M.; Bai, Q.; Wang, C.; Han, X. Design and Synthesis of Cu@CuS Yolk−Shell Structures with Enhanced Photocatalytic Activity. *Nano-Micro Lett.* **2017**, *9*, 35.